Vortex-induced vibrations of a circular cylinder with a pair of control rods of varying size

J.I. Jiménez-González[a,*], F. J. Huera-Huarte[b]

[a] *Departamento de Ingeniería Mecánica y Minera, Universidad de Jaén. Campus de las Lagunillas, 23071 Jaén, Spain.*
[b] *Department of Mechanical Engineering, Universitat Rovira i Virgili. 43007 Tarragona, Spain.*

Abstract

We present an experimental study on the vortex-induced vibration (VIV) of a low mass-damping one-degree-of-freedom circular cylinder subject to uniform cross-flow, with pairs of control rods of varying size located in its wake. Two particular locations for control rods, selected according to recent experimental maps of VIV sensitivity to localized perturbations, have been tested for increasing control rod diameters, d. Important amplitude reductions are observed for all arrangements investigated, with nearly total suppression of oscillations (up to 90%) for control rods of $d = 0.4D$, where D is the diameter of the main cylinder. Force measurements have been used to describe the nature of changes observed in the wake and the mechanisms behind the VIV control. In general, the placement of control rod pairs in the near wake leads to an important weakening of the lift coefficient and alters substantially the phase between transverse force and cylinder displacement. Moreover, it is shown that, for some particular arrangements, attenuation of VIV is obtained along with a drag reduction of approximately 60% at the upper branch of amplitude response, rendering the present strategy an interesting and practical solution for VIV control when several cylinders need to be installed together.

Keywords: Vortex-induced vibrations, cylinder wake, VIV, passive control.

1. Introduction

Vortex-induced vibrations (VIV) of cylindrical structures represent a classical problem in many engineering applications, such as offshore systems, where slender components, i.e. risers, pipelines or cables; are subjected to large hydrodynamic forces, that may entail strong vibrations and increase the risk of structural damage or fatigue failure. The nature of VIV of cylindrical components has been extensively investigated in the past, providing with a vast literature on the phenomenology and prediction of VIV (see e.g. [1–7]).

Besides, the aforementioned negative structural effects of VIV have given rise to a traditional interest on the mitigation of the VIV response by means of flow control techniques, that can be either active or passive [8], depending on whether there is power input or not. Passive strategies are generally easier to implement, and are based on geometrical modifications of the bluff body or perturbation of the near wake, being generally designed to influence separation and vortex shedding. Some of such classical strategies for cylindrical bodies were collected by Zdravkovich [9] or Blevins [10], and comprise, among others, the use of plates and fairings [11, 12] or helical strakes [13, 14], which have been proven efficient to reduce VIV response. However, the implementation of such techniques entails the deployment of add-on devices that could be expensive to install or maintain. On the other hand, there are many engineering applications prone to undergo VIV that involve several circular cylinders, whose interaction may modify strongly the system dynamic response. A classical example of systems where cylindrical bodies of different size exist are the piggyback pipelines or ensemble of secondary umbilicals and flowlines present in plenty of offshore oil and gas applications, where cylindrical bodies are clamped together at fixed clearances and along longitudinal intervals. Moreover, if these intervals are short enough, the whole arrangement may be treated as a unique, rigidly linked dynamical system.

*Corresponding author
Email addresses: jignacio@ujaen.es (J.I. Jiménez-González), francisco.huera@urv.cat (F. J. Huera-Huarte)

https://doi.org/10.1016/j.jsv.2018.06.002

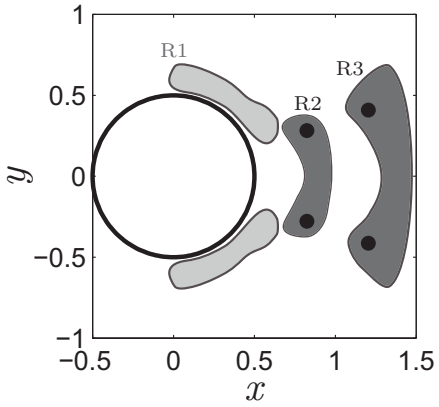

Figure 1: Sensitivity of VIV amplitude response for a flexibly mounted cylinder at Re = 13400 ($U^* = 6.3$): sketch of coherent regions where the placement of pairs of perturbation rods provides large VIV amplitude reductions, according to [25]. The dots within regions R2 and R3 correspond to those locations leading to weaker VIV responses, which are selected for the present study.

The location of secondary cylinders and the layout adopted are parameters that affect strongly the hydrodynamical forces, and therefore, the system VIV response. Thus, the search for *optimal* configurations of secondary cylinders aiming at reducing VIV amplitude, has been the goal of plenty of works, where smaller cylinders are commonly denoted as control rods. Most studies have investigated the effect of varying the azimuthal angle of rods around the main cylinder, and the gap between them, for different configurations and a given ratio between the diameters of main cylinder, D, and small ones, d. These studies have dealt with arrangements with a single rod [15], two rods [16–18], triangular and squared configurations of rods [19, 20], or even larger number [21], using either numerical or experimental approaches. Some of such studies have also evaluated the influence of flexibility of control rods on the VIV response, allowing to establish qualitative comparisons between rigid and flexible arrangements. For instance, the use of a symmetric arrangement with four flexible rods around a rigid cylinder was tested experimentally for turbulent flow regimes by Wu et al. [19], showing that cross-flow and in-line vibrations can be practically inhibited when the rods cover most of the main cylinder length. Similar qualitative results were numerically obtained by Zhu and Yao [21], using the same arrangement with rigid rods for a two-dimensional configuration and a similar range of Reynolds number. Thus, the use of rigid rods may simplify the analysis while providing with relevant results in terms of amplitude reduction. In general, these studies were based on a trial and error process and tackled the problem by means of parametric modifications of the arrangement, showing that the effect on the dynamic response is highly dependent on the layout and size of smaller rods, since both amplification or attenuation of VIV amplitude can be obtained.

One simple, efficient VIV control strategy consists actually in altering the vortex shedding process by placing the rods in the wake of the main cylinder, following the concept of wake control through localized perturbations. Thus, Strykowski and Sreenivasan [22] showed that the vortex-shedding behind a stationary cylinder can be effectively suppressed at low values of Reynolds numbers, if a small rod is properly placed in the regions of the wake which are more sensitive to forcing. The potential use of a control rod to cancel VIV could be inferred from the experimental works of Sakamoto and Haniu [23] and Dalton *et al.* [24], who showed the effectiveness of such technique to reduce the lift and drag due to vortex-shedding, by parametrically modifying the location of the rod at the wake of the main cylinder. More recently, Jiménez-González and Huera-Huarte [25] extended the concept of wake sensitivity to localized perturbations to one-degree-of-freedom VIV for an elastically mounted circular cylinder. An experimental sensitivity map of the near wake was obtained by parametrically modifying the position of a symmetric pair of perturbation rods, with $d = 0.03D$. The sketch in Fig. 1 depicts the main coherent region identified in [25], where the placement of a symmetric pair of perturbation rods leads to largest VIV amplitude reduction with respect to the uncontrolled natural VIV response of the cylinder at Re = 13400 (or reduced velocity $U^* = u_\infty / f_n D = 6.3$, being u_∞ the free-stream velocity and f_n the natural frequency of oscillation in still water). These regions were found along the cylinder's surface and in the near wake, for radial distances of $r \simeq 0.6D,\ 0.9D$ and $1.3D$ from the cylinder center, showing

by means of wake visualizations that different stabilizing mechanisms are related to alterations in the shear layer detachment, or the vortex formation process. Moreover, the effect of perturbation size was also evaluated using cylinders of $d = 0.1D$ instead, obtaining amplitude reductions up to 66% when *optimal* locations were selected according to sensitivity maps (although the improvement was seen to be highly dependent on U^*). The suitability of using these sensitivity distributions for the effective design of passive control systems, instead of carrying out a trial and error process, was later confirmed by Huera-Huarte [26], who observed a nearly total suppression of VIV amplitude by placing wired meshes around the cylinder, at the loci of highest sensitivity reported in Ref. [25] at $r \simeq 0.9D$ and $1.3D$ (corresponding to regions R2 and R3 in Fig. 1).

In view of those results, the present work aims at exploring the potential of sensitivity maps to design optimized arrangements of rigid piggyback pipelines of different sizes in terms of VIV. To that aim, we will study experimentally the dynamic response and fluid forces acting on distinct configurations with varying diameters ratios, rigidly connected and disposed according to loci of VIV amplitude reductions in aforementioned sensitivity maps. The analysis will focus on symmetric triangular arrangement, where a pair of control rods is located downstream of the main cylinder at *optimal* distances $r \simeq 0.9D$ and $1.3D$ [26]. The effect of the control rod size will be investigated by varying parametrically the diameters ratio d/D within the range $[0.1, 0.4]$, to assess if the stabilizing effect of localized wake perturbations is strengthened or, conversely, lessened as the control rod increases due to non-local, non-linear interaction mechanisms. Note that the use of symmetric arrangements constitutes a simplified approach, since risers ensembles in real applications can be also misaligned with respect to the flow stream, what could also lead to enhancement of vibrations. However, in spite of such limitation, the use of symmetric layouts will allow to gain insight into the general controllability of the VIV and forces by means of near wake modifications, while providing with dynamics responses without any mean lift component, as it would be the case of asymmetric arrangements. That said, the paper is organized as follows: the experimental aspects are first described in Sect. 2; while results of dynamic response obtained from tests conducted at different reduced velocities are presented in Sect. 3. Next, the wake forcing is studied at Sect. 4 by analyzing measured force distributions and corresponding frequencies. Finally, the main conclusions of the research are drawn in Sect. 5.

2. Problem description and experimental set-up

Fig. 2 displays schematic representations of the experimental set-up, which consisted of arrangements with a main cylinder, of diameters D, and control cylinders of diameters d, whose centers are located at positions $(r, \pm\theta)$, relative to the coordinate system defined by the oscillating cylinder, as seen in Fig. 2(c). Two *optimal* layouts were tested (Fig. 2c), aside from the isolated plain cylinder, namely: configuration #1 where a pair of control cylinders was placed at positions $(r, \pm\theta) = (0.9D, 20^{\text{o}})$, and configuration #2 with the rods located at $(r, \pm\theta) = (1.3D, 20^{\text{o}})$. Besides, for each configuration, four different diameters of control rods have been studied, i.e. $d/D = [0.12, 0.2, 0.32, 0.4]$.

Experimental tests were carried out in the Free Surface Water Channel (FSWC) of the Department of Mechanical Engineering at Universitat Rovira i Virgili (URV). The facility consists of a recirculating channel with a test section of 1×1.1 m^2, able to deliver a free-stream axial velocity u_∞ up to 0.6 m/s, with a maximum variability of 1.6%, when the water height is 1 m. The cylinder model was made of a rigid acrylic tube of $D = 0.05$ m and submerged length $L = 0.53$ m, providing an aspect ratio $L/D = 11$. Aluminum tubes of smaller diameters were disposed as the downstream control cylinders, and were held using 3D printed slim parts that were located at the upper and bottom ends of the main cylinder (Fig. 2b). An end plate was also attached at the bottom to avoid any three-dimensional effect from flow detachment at the cylinder base. As depicted in Fig. 2(a), the whole system was elastically mounted in a rigid structural frame and hung from a one-degree-of-freedom air-fed linear slide, which restricted the oscillating motion of the system to the cross-flow y-direction, whose displacement was measured by means of a laser displacement sensor. Besides, the flow forces acting on the cylinder along the cross-flow and in-line directions were measured in two ways. First, a multi-axial load cell, with a measuring range of 100N, was installed between the air bearing rig and the system, being primarily employed to measure the in-line force acting on the system, as will be detailed in Sect. 3. Additionally, a precision uni-axial S-Beam load cell with a measurement range of 8.9 N, was installed between the primary rig and a secondary sliding carriage, displacing alongside the oscillating assembly, to accurately measure the cross-flow force with a second independent sensor, for redundancy.

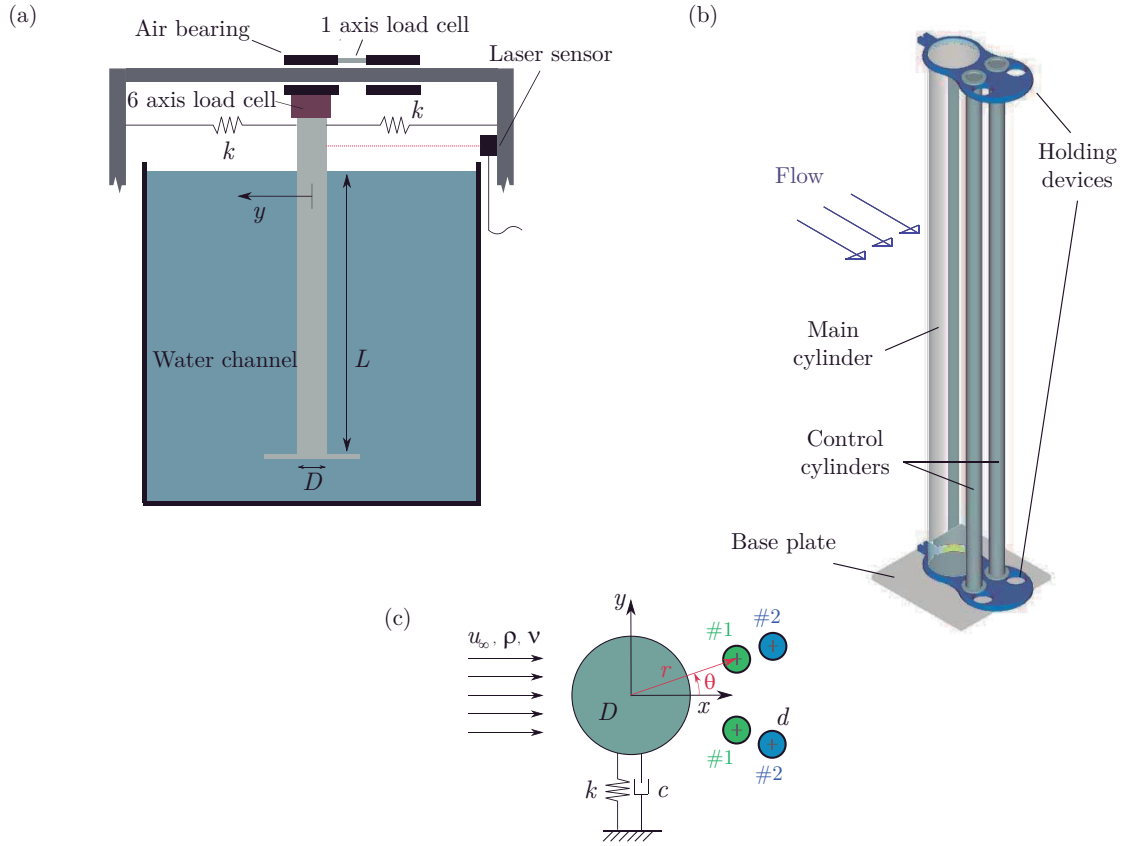

Figure 2: Experimental set-up: (a) sketch of water channel facility and (b) detailed view of control system. (c) Scheme of the problem.

The structural parameters characterizing the problem are the mass ratio, m^*, and the structural damping, ξ. Considering the control cylinders, the former is defined as

$$m^* = \frac{4(m + 2m_c)}{\pi\rho L(D^2 + 2d^2)}, \tag{1}$$

where m corresponds to the mass of the main cylinder ensemble, including the holding devices and load cell, while m_c stands for the mass of control rod with diameter d. Table 1 lists values of m^* for the different arrangements investigated, along with the combined mass-damping parameter $m^*\xi$. In that sense, an averaged value of m_c has been used to determine the structural damping in air by means of free-decay tests, which was found to be $\xi = 0.0035$. The natural frequency of oscillation in still water, f_n, is also characterized for each arrangement and displayed in Table 1 with regard to the uncontrolled plain cylinder case, f_{n0}. Besides, the Reynolds number, defined as $\mathrm{Re} = u_\infty D/\nu$, where u_∞ and ν are respectively the free-stream velocity and kinematic viscosity, ranged from 6000 to 32000. Similarly, the reduced velocity, defined as $U^* = u_\infty/f_n D$, covered approximately the range from 4 to 12 (note that values depend on the control rod assembly).

The y displacement and the forces acting on the cylinder were collected using a data acquisition system with a sampling frequency of $F_s = 1.6$ kHz during 90 s, to ensure enough temporal resolution and to accurately capture the system dynamics (note that at least 45 oscillation cycles were recorded for each test presented in following sections).

3. Dynamic response of controlled system

We first present the dynamic response of the different control rod arrangements investigated, which are compared to that corresponding the plain cylinder. The VIV dynamic response is characterized by the os-

Set-up	m^*	$m^*\xi$	f_n/f_{n0}
plain cylinder	2.68	0.0094	-
$d/D = 0.12$	2.66	0.0093	1.00
$d/D = 0.2$	2.58	0.0091	0.99
$d/D = 0.32$	2.37	0.0083	0.97
$d/D = 0.4$	2.21	0.0079	0.95

Table 1: Structural properties of the different configurations studied in the present work: mass ratio, m^*, mass-damping ratio, $m^*\xi$ and ratio of natural frequencies in still water with respect to the plain cylinder case, f_n/f_{n0}.

cillation amplitude A and frequency f, which are nondimensionalized using respectively the main cylinder diameter, D, and the natural frequency of the corresponding assembly under study, f_n (see Table 1), to give $A^* = A/D$ and $f^* = f/f_n$. Spectral analysis of time signals allows determination of frequencies and amplitudes. In particular, the latter is obtained by means of integration of the peak in the Power Spectral Density distribution, PSD(F^*), associated with the fundamental frequency f^*, in such a way that

$$A^{*2} = 2 \int_{f^*-\Delta f_d^*}^{f^*+\Delta f_u^*} \mathrm{PSD}(F^*)\, \mathrm{d}F^*, \tag{2}$$

where Δf_d^* and Δf_u^* stand for the interval around f^* for which the energy drops to 1% the peak value, and F^* represents the frequency values spanning the interval $[0, F_s^*/2]$. Note that this method provides with estimations of A^* which are nearly identical to those computed as the mean of instantaneous amplitude calculated by means of the Hilbert transform of the measured displacement signal.

Let us first discuss qualitatively, the effect of control configurations #1 and #2 for increasing diameter ratio d/D on the dynamic response of the flexibly mounted system, at a particular value of $U^* \simeq 6.2$ (Re $\simeq 13900$), in which very energetic oscillations were observed. Fig. 3 presents temporal evolutions of amplitude response $A^*(t)$, and corresponding Power Spectral Density function, PSD(F^*), for the *optimal* layout selected, #1 (Figs. 3a-b) and #2 (Figs. 3c-d), and different control diameters ratios. At the selected value of U^*, the amplitude of the plain cylinder is $A_0^* \simeq 0.99$ (see dashed horizontal lines), which agrees with values of largest amplitude in previous works describing the VIV of low mass-damping circular cylinders (see e.g. Ref. [27]). Note that, for the uncontrolled plain case, the peaks of temporal amplitude response are slightly bumpy due to the modulation of the amplitude and the existence of several harmonics components at $U^* \simeq 6.2$. The effect of increasing the parameter d/D contributes positively to reduce the amplitude of oscillations for both layouts, although apparently, it is more efficient for the first configuration, for which there is an abrupt decrease of A^* and the main peak in the PSD(F^*), for $d/D > 0.12$. This sharp change suggests a general qualitative modification in the regime of dynamic response. Besides, the attenuation of oscillations seems to be more progressive with d/D for configuration #2.

The complete curves of amplitude and frequency responses with respect to reduced velocity U^*, and Reynolds number Re, are depicted in Figs. 4 and 5 for both layouts #1 and #2, respectively. The response of the single plain cylinder is also included for comparison. This uncontrolled case shows the classical curve for VIV of flexibly mounted cylinders in water, consisting of initial, upper and lower branches, being largest amplitudes reached within the upper branch ($A_0^* \simeq 1$). The oscillation frequency (see Fig. 4b) grows linearly as U^* is increased along the initial branch, following the Strouhal law ($St \simeq 0.18$), to reach a plateau within the upper branch, that indicates the beginning of the *lock-in* range.

The placement of control rods of increasing size alters substantially the dynamic response of the flexibly mounted system. When configuration #1 is selected (Fig. 4), increasing the control diameter produces a progressive overall reduction of A^*, although the type of response is highly dependent on the value of d/D. For instance, when $d/D = 0.12$, the response is qualitatively similar to that of the uncontrolled case, with well defined branches, although the range of VIV response narrows (oscillations occur for $U^* \lesssim 11$). Moreover, an important amplitude weakening is observed at the initial and the upper branches. For $d/D > 0.12$ the picture is qualitatively different, since the upper branch seems to be inhibited. In particular, for $d/D = 0.2$, there is a growing trend in the amplitude up to $U^* \simeq 7$, where a nearly constant value of $A^* \simeq 0.47$ is reached, that is followed by a monotonous decay in A^* within the range $9 \lesssim U^* \lesssim 11$. A similar picture is observed

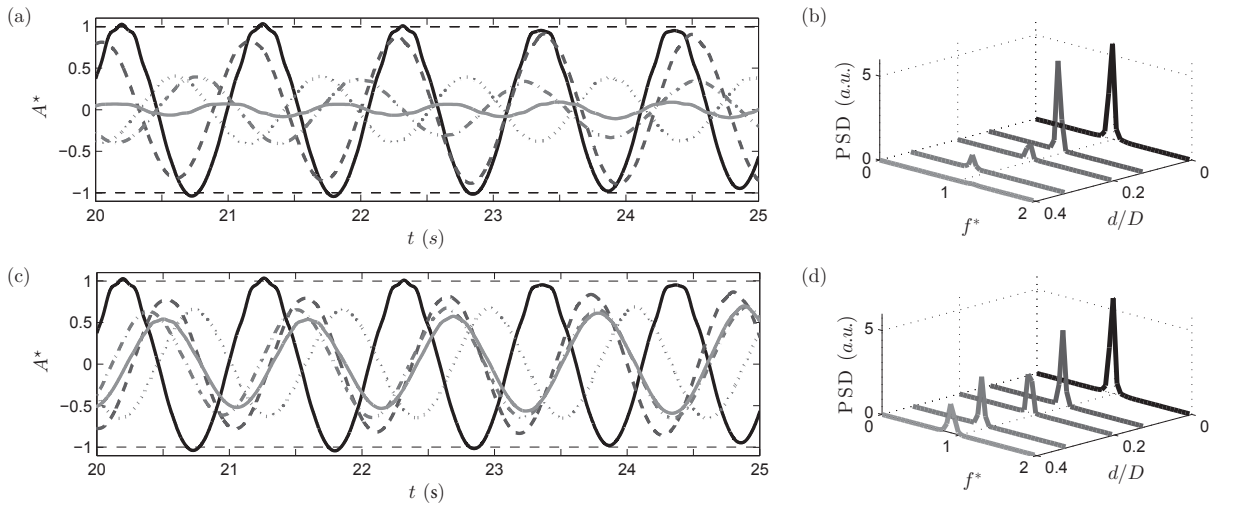

Figure 3: Temporal amplitude response $A^*(t)$ (a,c) and corresponding Power Spectral Density function, PSD(F^*) (b,d), for configuration #1 (a-b) and #2 (c-d), with different diameters ratios d/D, at $U^* \simeq 6.2$ (Re $\simeq 13900$). In temporal signals: black solid line (plain cylinder), gray dashed line ($d/D = 0.12$), gray dotted line ($d/D = 0.2$), gray dashed-dotted line ($d/D = 0.32$) and gray solid line ($d/D = 0.4$). Dashed horizontal lines represent the value of uncontrolled amplitude A_0^*.

for $d/D = 0.32$, although now the response at lower branch is further extended to higher values of U^*. Note that, as showed in Table 1, increasing the value of d/D with this set-up led to reduction of m^* values, what is known to widen the synchronization range and to extend it to larger values of U^* (see e.g. Ref. [28]). Finally, for $d/D = 0.4$ a nearly total VIV suppression takes place for reduced velocities lower than 8, although the amplitude keeps growing for larger values of U^*, extending the range of VIV response. Nevertheless, the value of A^* remains always below those from the uncontrolled case at the lower branch. These results show that a maximum amplitude reduction of nearly 90% can be obtained at the upper branch if control rods are sufficiently large.

Oscillation frequencies behave in a similar manner to the uncontrolled reference case, although the beginning of the lock-in regime shifts slightly leftwards as d/D increases (see Fig. 4b). This trend is however different for $d/D = 0.4$, for which there is a jump around $U^* = 7.5$ which marks the start of the growing trend in A^* and corresponds to the lock-in regime. In that case, one could infer that the initial branch widens while the upper one vanishes. Besides, the oscillation frequency during the lock-in range decreases, and for $d/D = 0.4$ it never exceeds the natural frequency f_n. Note also that there is an overall slight shift in U^* for all curves, as a consequence of the natural frequency growth occurring when the parameter d/D is increased (see Table 1).

Corresponding VIV responses for the flexibly-mounted controlled systems with layout #2 are shown in Fig. 5. The first feature to remark is the progressive mitigation of VIV amplitude as d/D grows, alongside the narrowing and rightwards shift of the upper branch response. In general, A^* curves are qualitatively similar for all the arrangements investigated, since they present well defined branches, although for $d/D \geq 0.32$ there is marked transition between an initial branch of attenuated amplitude and nearly constant value, and the response of maximum displacement within the modified upper branch. The amplitude reduction attained when the maxima in the curves takes place in the upper branches is near 40%. In addition, oscillation frequencies (Fig. 5b) are very similar for all the systems implemented, with only slight changes when the control rod diameter is increased.

The overall dependence of VIV amplitude with the reduced velocity and the diameters ratio is summarized in Fig. 6, where the three-dimensional amplitude plots (Figs. 6a-b) and their corresponding two-dimensional contours of amplitude response (Figs. 6c-d) are displayed for both configurations #1 and #2. Note that the data of amplitude response depicted in contours of Figs. 6(c-d) for values of d/D not tested in the present analysis, have been interpolated from measured cases. As mentioned, increasing the value of d/D in both layouts implies the progressive reduction of A^*, especially within the upper branch, where largest displacements occur for the uncontrolled case, although different behaviours are observed depending on the layout. For

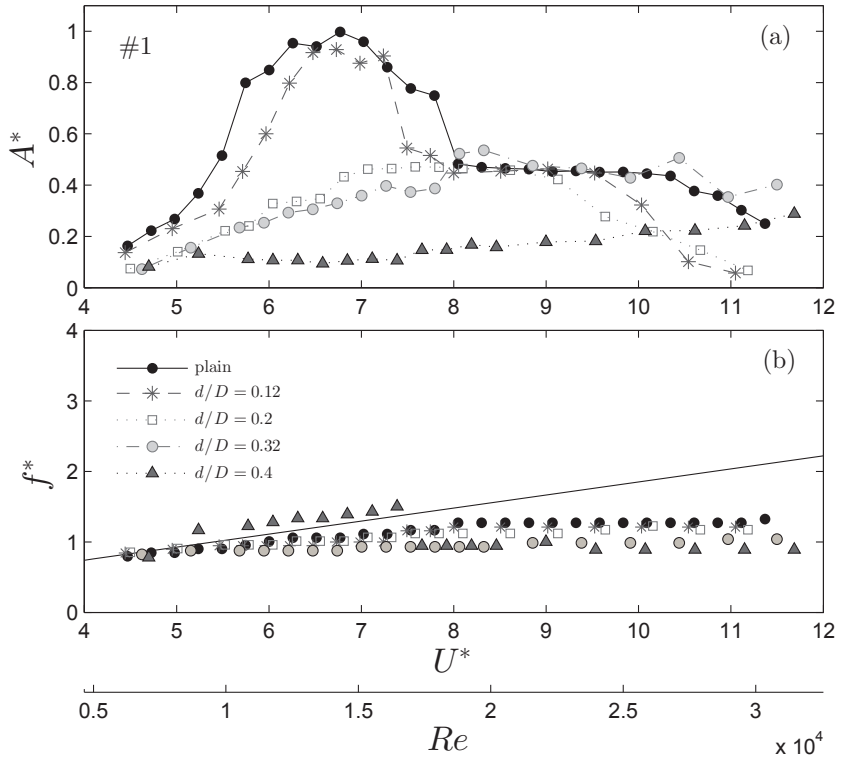

Figure 4: (a) Amplitude and (b) frequency response of the flexibly-mounted systems of different d/D with layout #1, versus reduced velocity U_r and Reynolds number Re. VIV response for isolated plain cylinder is included for comparison.

instance, for the first case (Figs. 6a,c), three types of responses can be described based on amplitude results. Thus, when $d/D \leq 0.12$ curves are characterized by well defined response branches, whereas for $0.12 < d/D \leq 0.32$, the initial branch extends towards larger values of U^*, softly leading to a plateau in the amplitude, which seems to be the outcome of the upper and lower branches merging. Finally, for $d/D = 0.4$, there is a practically total suppression of oscillations at the upper branch, where amplitude reductions of nearly 90% are obtained. Conversely, for arrangements based on configuration #2 (Fig. 6b), the controlled dynamics varies smoothly with d/D, being characterized by distinguishable lower and upper branches, where amplitude magnitude decreases progressively. However, it is worth highlighting that, when $d/D \geq 0.32$, an initial branch of nearly constant small amplitude develops.

The installation of control rods of increasing size has been shown to lead to mitigated or partially suppressed oscillations over a wide range of reduced velocity, with the cylinder responding generally over a narrow range of U^*. This controlled dynamics will be subsequently analyzed based on the force coefficients and the phase difference between the forcing and the response, which will also help shedding some light on the control mechanisms acting here.

4. Force measurements of controlled systems

4.1. Validation of measured data

As mentioned in Sect. 2, both a multi-axial and a uni-axial load cell were used to investigate the forces in the cross-flow direction (F_y). Instantaneous values of in-line force, $F_x(t)$, measured with the multi-axis load cell, were found to be always close to 5N, which represents a 5% of the full scale of the multi-axial sensor. This was considered appropriate for calculating the time-averaged drag coefficients, provided this was the only way of measuring them in the experimental system designed. However, maximum values of instantaneous

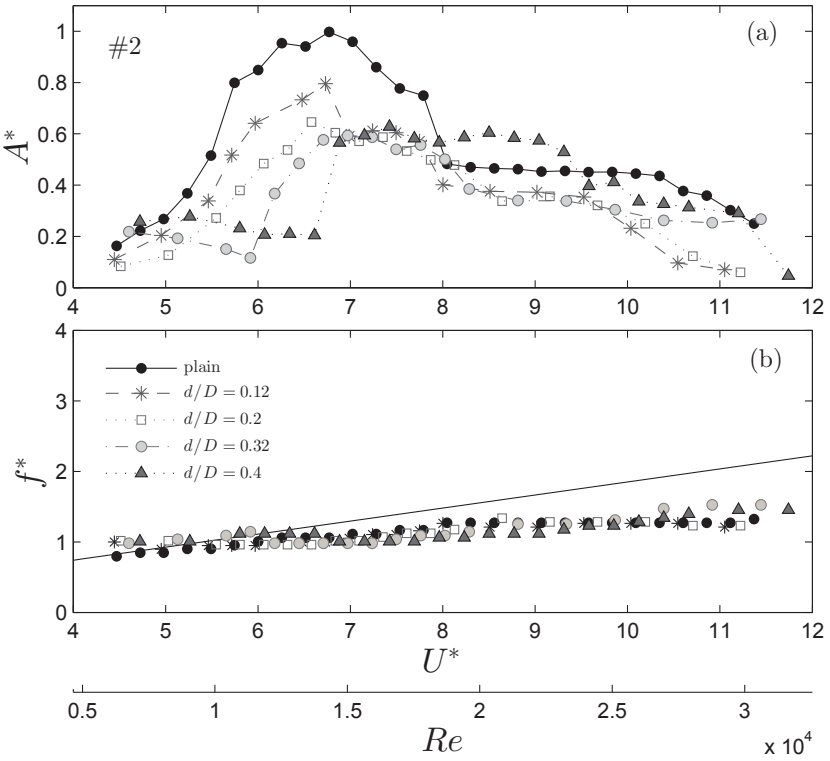

Figure 5: (a) Amplitude and (b) frequency response of the flexibly-mounted systems of different d/D with layout #2, versus reduced velocity U_r and Reynolds number Re. VIV response for isolated plain cylinder is included for comparison.

cross-flow force magnitude did not exceed 2N for the present experiments and therefore a second redundant load cell was used to validate the results. In fact, since the major interest was in the amplitude of the cross-flow force variations, the uni-axial load cell measurements were finally used, giving larger resolution. Moreover, the measured transverse force is validated by using the displacement y and modeling the structure as a one-degree-of-freedom system, which is a widely accepted method in the literature (see Refs. [27, 29]). This process will also serve to illustrate the mentioned drawback and to justify the use of two force sensors in the present work. Following the previous assumption, the cross-flow force can be computed as:

$$F_y = m\ddot{y} + 2m\omega\xi\dot{y} + m\omega^2 y, \tag{3}$$

where m is the mass of the moving system (which depends on the control rods used), ξ the structural damping (0.0035 for the averaged set-up), ω is the system angular oscillation frequency and y the displacement measured by means of the optical position sensor. A validation case is presented in Fig. 7, where computed and measured cross-flow force values are compared for the plain cylinder, at $U^* \simeq 5.0$, 6.0 and 10.2, which correspond respectively to points in the initial, upper and lower branches of the response curve. Measured data from load cells was post-processed to subtract the inertia force related to the motion of the corresponding oscillating mass. As it can be observed, both the computed time evolution of F_y and its corresponding spectra, reproduce accurately the force signal measured through the uni-axial load cell for the three cases selected. However, as initially suspected, the small magnitude of the force amplitude does not allow a perfect match between the forces coming out of the multi-axial sensor and the other two methods. Note also that, although carefully mounted and aligned, a small misalignment of the end plate could result into small off-axis forces that may have increased the error between measurements from both force sensors. Therefore, only the values of cross-flow force measured by means of the uni-axial load cell will be used in the following. Again, time-averaged values of in-line forces are only available as measured by the multi-axis sensor.

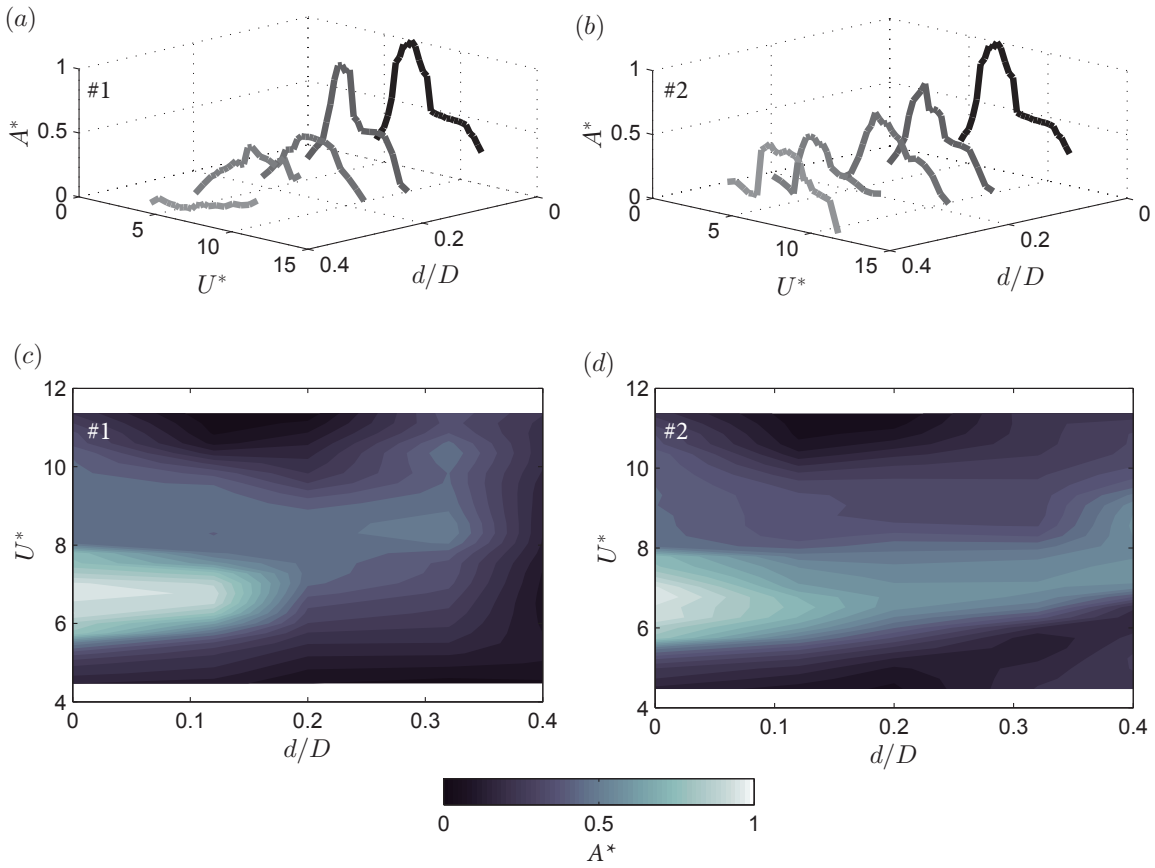

Figure 6: (a-b) Plots of amplitude response as a function of the reduced velocity U^* and diameters ratio d/D, for configurations #1 and #2; and (c-d) corresponding contours of amplitude response for the same respective configurations. Data in (c-d) have been interpolated from measured results.

4.2. Lift coefficient and phase between force and displacement

The lift coefficient amplitude is computed as

$$C_y = \frac{\hat{F}_y}{0.5\rho DLu_\infty^2}; \tag{4}$$

where $\hat{F}_y = \sqrt{2}F_{y,rms}$, and rms stands for the root mean square value of the fluctuating cross-flow force. The lift coefficient can be divided into components in phase with the acceleration, $C_{y,a}$, and with the velocity, $C_{y,u}$. Such coefficients were computed as the time-average of the product between the instantaneous value of the cross-flow fluctuations about its mean value, with the displacement and velocity respectively, namely $C_{y,a} = \overline{C'_{y,a}}$ and $C_{y,u} = \overline{C'_{y,u}}$. The fluctuating values $C'_{y,a}$ and $C'_{y,u}$ were respectively obtained by means of the following expressions [30]:

$$C'_{y,a} = \frac{\sqrt{2}\left(F_y - \overline{F_y}\right)}{0.5\rho DLu_\infty^2} \frac{y}{\sqrt{\bar{y}^2}}, \tag{5}$$

and

$$C'_{y,u} = \frac{\sqrt{2}\left(F_y - \overline{F_y}\right)}{0.5\rho DLu_\infty^2} \frac{\dot{y}}{\sqrt{\bar{\dot{y}}^2}}. \tag{6}$$

Thus, positive values of $C_{y,u}$ indicate a net transfer from the fluid to the body, what excites the structural response. Besides, the phase difference between the y displacement and the lift force ϕ was obtained using the Hilbert transform,

$$\phi = \phi_{F_y} - \phi_y. \tag{7}$$

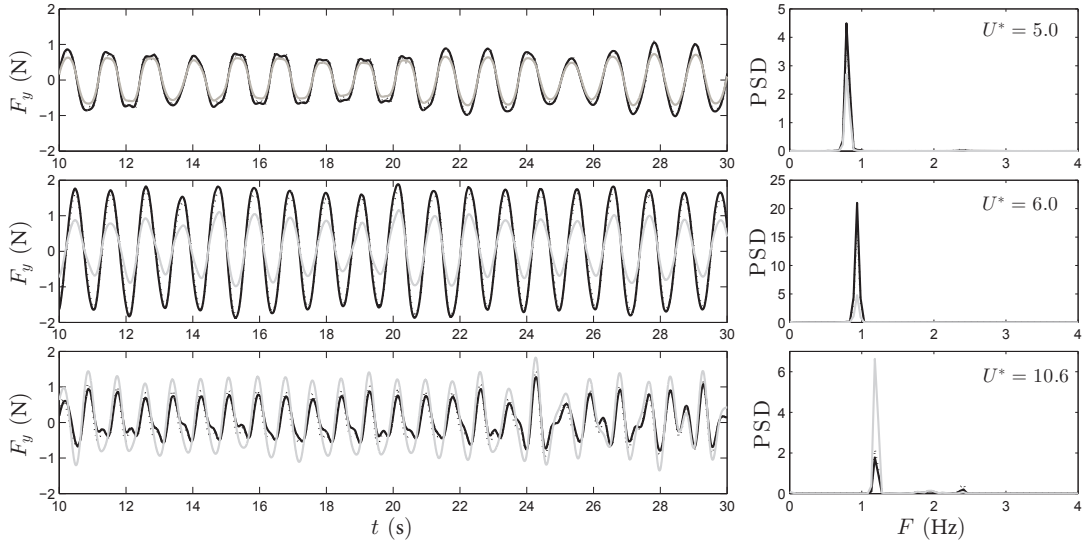

Figure 7: Temporal evolutions of cross-flow force, $F_y(t)$, and their corresponding power spectral density, PSD(F), measured directly using the uni-axial load cell (black solid line), the multiaxial load cell (gray solid line), and reconstructed using the model of Eq. 3 (black dotted line), for the plain cylinder at $U^* = 5.0$, 6.0 and 10.6.

Fig. 8 depicts lift coefficient amplitude and corresponding components, together with the phase difference, for the different ratios d/D based on layout #1 and the plain cylinder, which will be first analyzed to set a reference. First, the lift coefficient peaks approximately at $U^* \simeq 5.7$ (see Fig. 8a), that corresponds to the amplitude jump between initial and upper branches in Fig. 4(a). After that, a monotonous decrease is observed for C_y with U^* growing, until reaching a nearly nil asymptotic value as the VIV response decays in amplitude. The lift components in phase with velocity, $C_{y,u}$, presents positive values for all U^*, reaching a maximum at $U^* \simeq 6.5$, close to the maximum of amplitude response in Fig. 4(a). As said, the coefficient $C_{y,u}$ is related to the fluid damping, and quantifies the energy transfered from the fluid to the body. Therefore, the largest excitation is obtained when $C_{y,u}$ reaches the maximum absolute value. Besides, $C_{y,a}$, which is related to the fluid inertia, peaks approximately at $U^* \simeq 5.7$ as C_y, and decreases until reaching a negative value for $U^* \simeq 8.0$, where the phase changes from 0° to 180° (Fig. 8d). This phase shift occurs when the oscillating frequency reaches the natural one in still water, i.e. $f^* \simeq 1$ (Fig. 4b), and corresponds to the decrease in A^* from upper to lower branch, since now the force acts in the opposite direction to the body's motion, and consequently, the response is weakened.

When the control rods of $d/D = 0.12$ are placed behind the cylinder model, force coefficients are slightly modified with respect to those of the plain case, but present similar trends, as it could have been expected from the VIV response displayed in Fig. 5. Main differences are related to weaker values of total lift C_y and component $C_{y,u}$, whose peaks are now shifted rightwards. Besides, $C_{y,a}$ is shown to become negative earlier than for the plain case, i.e. around $U^* \simeq 7.5$, corresponding to the phase difference jump (Fig. 8d) and the transition between upper and lower branches in amplitude response curve (Fig. 4a). In general, the combination of a sooner phase difference transition and weaker excitation and inertia lift components, $C_{y,u}$ and $C_{y,a}$, provides with a less energetic VIV response.

A further increase of control rods size up to $d/D = 0.2$, reduces significantly the total lift magnitude, C_y, which becomes nearly zero for $U^* > 7.5$, after peaking at approximately $U^* = 6.1$, where the inertia term, $C_{y,a}$, reaches also the largest value. This coefficient becomes negative now around $U^* = 9.1$, coinciding with the phase jump in Fig. 8(c). Interestingly, the phase difference changes now through 90° towards 0° again as the reduced velocity increases. This fact is counterbalanced by a low lift excitation component, $C_{y,u}$, which is now weaker than for smaller control rods, reaching its minimum around $U^* = 7.6$, where the amplitude of motion A^* is also largest in Fig. 4(a). From this point, both the amplitude response and the magnitude of $C_{y,u}$ decrease towards zero.

On the other hand, as it can be seen in Figs. 6(a,c), amplitude responses of $d/D = 0.2$ and 0.32 present

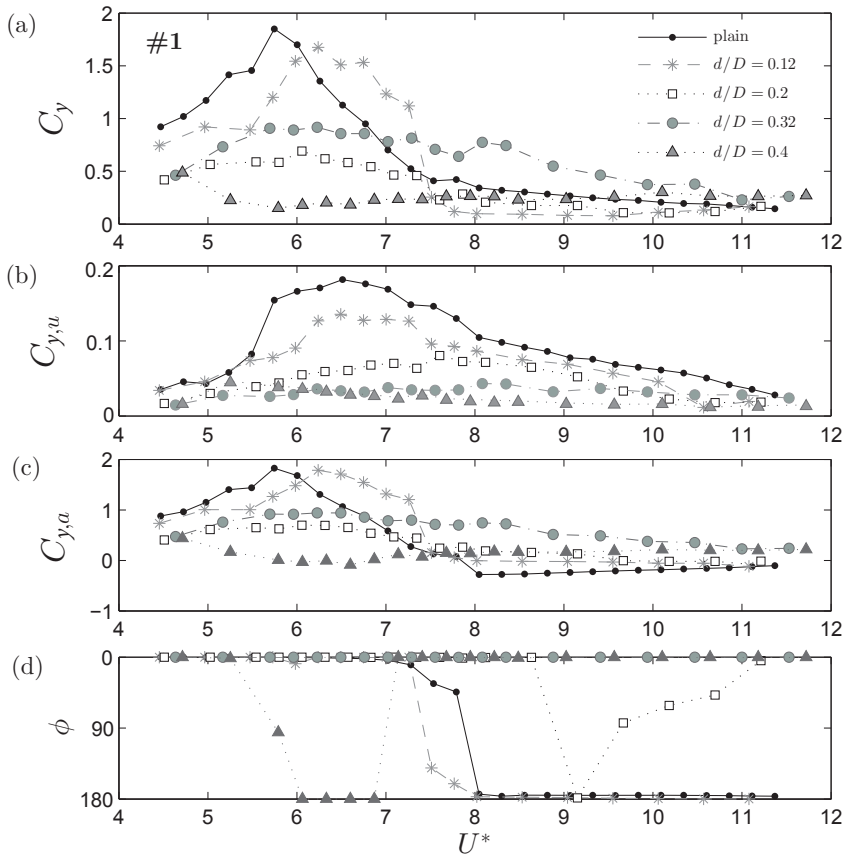

Figure 8: (a) Lift coefficient, C_y, along with corresponding components in phase with velocity (b) and displacement (c), and phase difference between lift and $y-$displacement (d), for different arrangements with layout #1.

qualitatively similar trends for $U^* < 9$, whereby A^* grows almost linearly for low values of reduced velocity, until reaching nearly similar constant amplitudes. However, the arrangement of $d/D = 0.32$ displays a larger amplitude response at higher values of reduced velocity. This behavior is the outcome of a larger magnitude of total lift C_y for the whole range of reduced velocity investigated. Moreover, the lift component in-phase with velocity $C_{y,v}$ lies very close to zero, indicating that the forcing is basically guided by the component $C_{y,a}$ in-phase with acceleration, which now is always positive and above the curve of $d/D = 0.2$. Thus, the phase angle ϕ never shifts from 0^o to 180^o meaning that, even at larger values of reduced velocity, the forcing acts in the same direction as the body displacement and the level of motion amplitude is somehow maintained.

Finally, for the largest control rod size investigated, i.e. $d/D = 0.4$, the system response is largely attenuated as a consequence of a very low total lift coefficient C_y and corresponding components over the entire range of reduced velocity. The magnitude of C_y (and $C_{y,a}$) is highest at the lowest value of U^*, from which it drops and then grows slightly for $U^* > 6$. The coefficient $C_{y,a}$ is negative around $6 < U^* < 7$, where the phase ϕ becomes 180^o, to subsequently jump back to 0^o. Meanwhile, $C_{y,u}$ remains close to zero over the entire range of U^*. The overall weak forcing translates into a very mitigated response for all U^* investigated.

Results with the forcing for #2 are displayed in Fig. 9 for different values of d/D. In general, unlike in the case of configuration #1, now both the lift and phase difference show clear trends as the control rod diameter grows, displaying progressive changes, what could be related to smooth, less abrupt, qualitative modifications in the wake. Thus, the decrease in the amplitude response reported in Sect. 3 (see Fig. 5a), is related to a reduction of the magnitude of total lift C_y and its components, $C_{y,a}$ and $C_{y,u}$ (Figs. 9a-c). In particular, the coefficient in-phase with the velocity $C_{y,u}$ (Figs. 9b) becomes smaller, thus reducing the excitation on the structure as d/D grows, whereas the coefficient in-phase with acceleration $C_{y,a}$ (Figs. 9c), presents a similar behavior to the total lift, with a progressive magnitude peak reduction and displacement towards larger values

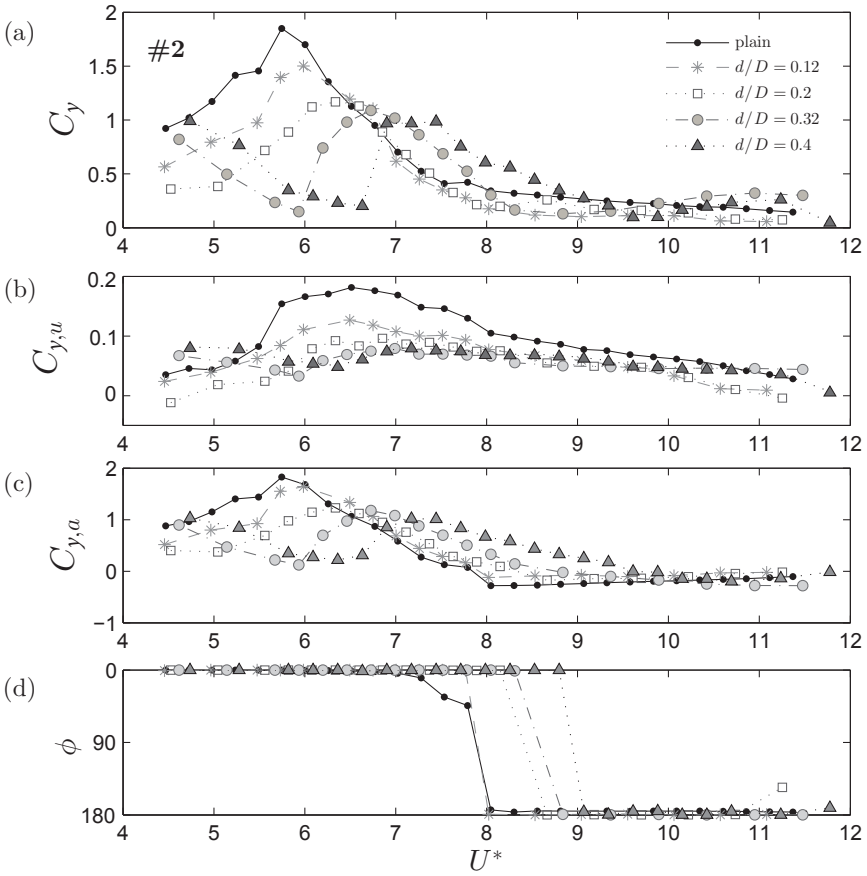

Figure 9: (a) Lift coefficient, C_y, along with corresponding components in phase with velocity (b) and displacement (c), and phase difference between lift and $y-$displacement (d), for different arrangements with layout #2.

of reduced velocity. Besides, the value of U^* for which $C_{y,a}$ becomes negative increases progressively, and consequently, the phase jump in Fig. 9(d) also moves slightly towards higher values of reduced velocity with d/D. This indicates that forcing and response are in phase for a wider range of reduced velocity for biggest values of d/D. This fact combined with the stronger magnitude of lift at larger values of U^* (due to shift in curves of C_y and $C_{y,a}$) leads to the rightwards extension of the upper branch curves of amplitude (Fig. 5a), what is particularly noticeable for $d/D = 0.4$ (for instance, the upper limit of such branch, which is determined by the phase jump, takes place around $U^* = 9$ approximately while for the uncontrolled case it occurs around 8). Additionally, for $d/D \geq 0.32$ and low values of reduced velocity ($U^* < 7$), the forcing is qualitatively different to that controlled configurations with $d/D = 0.12$ and 0.2, since there is a noteworthy growth in magnitudes of total lift C_y and coefficients $C_{y,u}$ and $C_{y,a}$. This distinct behavior translates into a more energetic response in terms of amplitude, as it was shown in Fig. 4(a), where a new initial branch was reported. Note that the frequency response for this range of reduced velocities is characterized by values of $f^* \simeq 1$, suggesting that there might be a widening of the lock-in range as d/D grows.

4.3. Correspondence between frequency forcing and response

Following the latter observation, we will next analyze the general modifications undergone by the structural dominant frequencies (response frequency) and the cross-flow forces (forcing frequency) upon increases of the control rod sizes. Fig. 10 displays PSD spectra from cross-flow force signals along with their corresponding dominant forcing and oscillation frequencies, for the plain cylinder case (Fig. 10a) and both controlled configurations, #1 (Fig. 10b) and #2 (Fig. 10c), for control rods size $d/D = 0.12$, 0.2 and 0.4. Power spectra are used here to qualitatively estimate the intensity of wake oscillations and coherence of vortex shedding. As it is shown in Fig. 10(a), the plain cylinder case is characterized by a response frequency which is coincident with

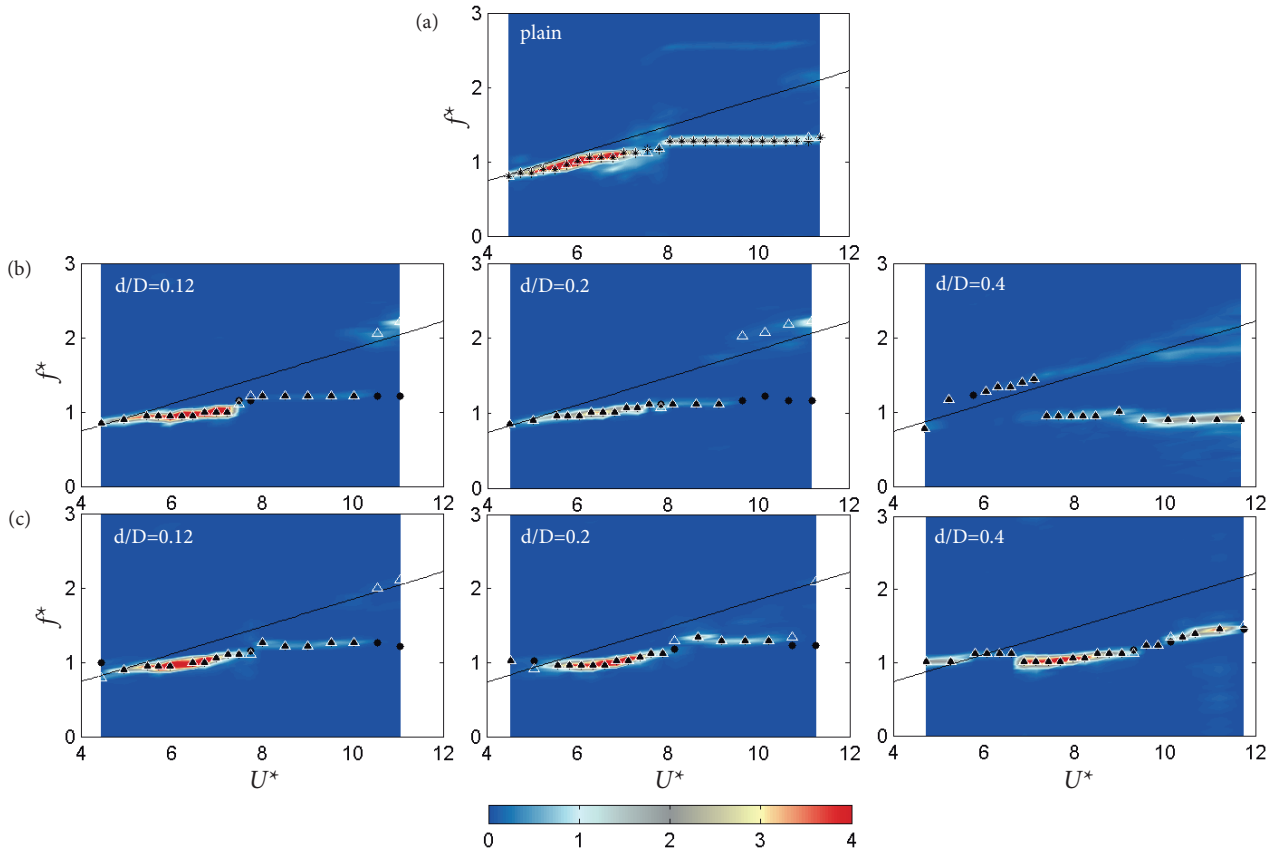

Figure 10: PSD spectra of cross-flow force signals (background contours) and corresponding dominant forcing frequency (white triangle symbols) and response oscillation frequency (black dotted symbols) for: plain cylinder (a) and controlled configurations #1 (b) and #2 (c), with control rods size $d/D = 0.12$, 0.2 and 0.4. Solid lines represent the Strouhal law with $St = 0.18$, while the colormap indicates value of PSD amplitude of cross-flow force.

the dominant forcing frequency for the whole range of reduced velocity investigated. Thus, the initial branch is shown to be characterized by growing frequencies that follow the Strouhal law (solid line in Fig. 10 represents a measured value of $S \simeq 0.18$), until a point where the oscillations in the wake attain its largest magnitude, from which frequencies start to level off, with $f^* \simeq 1$, thus marking the beginning of the upper branch. For values of U^* between 7 and 8, the magnitude of PSD decreases and spectra display broader peaks, which is a known feature of the transition region between upper and lower branches, as it was previously reported by Khalak and Williamson [27] relating it to the change in wake regime between the so-called 2S and 2P modes. In view of the results, this transition between upper and lower branches takes place around $U^* = 8$, where the dominant frequencies reach a plateau at $f^* > 1$ (as it typically occurs for flexibly mounted cylinders with low $m^*\xi$ ratios). At the lower branch, the magnitude of PSD decreases and more periodic spectra with thinner peaks are observed, what may be related to the definitive setting of a 2P mode in the wake [28].

The implementation of control rods using layout #1 (Fig. 10b) produces significative changes in the wake and therefore, the forcing. First, when $d/D = 0.12$, there is general reduction on the magnitude of the PSD periodogram along with a shortening of the lower branch, when compared to plain case. Thus, forcing and response frequencies desynchronize for $U^* > 10$, where the forcing frequency follows the Strouhal law again. The modifications, although qualitatively similar, are more substantive in the case of $d/D = 0.2$, for which the desynchronization of frequencies values takes place at a lower reduced velocity. However, the picture is considerably different for $d/D = 0.4$. Now, the forcing and response frequencies follow the Strouhal law up to $U^* \simeq 7$, coinciding with a phase $\phi = 180^o$ and a very attenuated amplitude response (see Figs. 4a and 8d). Then, an abrupt transition takes place towards a plateau that is characterized by $f^* < 1$, from which the phase was shown to return to $\phi = 0^o$ (Fig. 8d) and the amplitude recovers (Fig. 4a). Besides, the forces spectra are

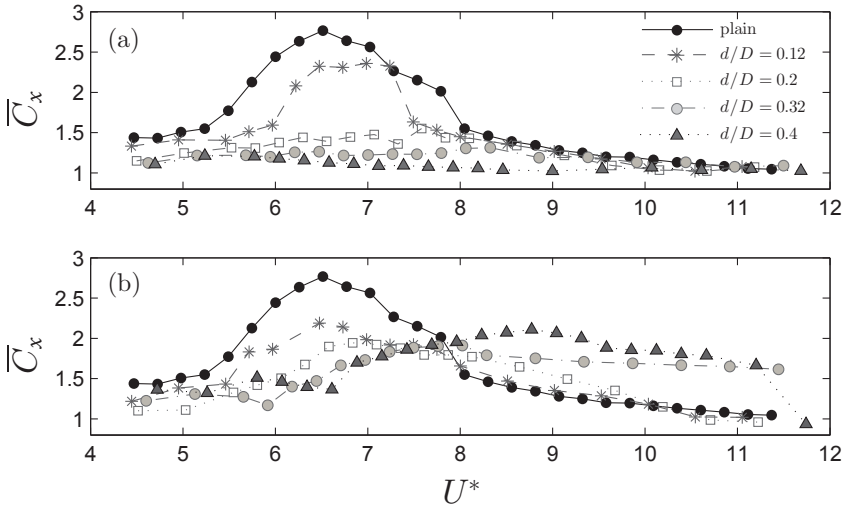

Figure 11: Mean drag coefficient, $\overline{C}_x$, as a function of reduced velocity U^*, controlled systems of different d/D and configurations #1 (a) and #2 (b).

now less periodic and present several peaks of similar order of magnitude (except for the initial branch). Unlike the previous cases, now the typical natural wake vortex shedding frequency is always observable in the spectra, also during the lock-in range, which seems to extend further than $U^* = 12$ (which was the experimental feasible limit of our study).

It is worth noting that there is a clear frequency decrease for the lock-in range as d/D grows, which is intrinsically related to wake modifications induced by control rods (note that, as listed in Table 1, the natural frequency of oscillations in still water f_n decreases with experimental arrangements of increasing d/D, and consequently values of $f^* = f/f_n$ can only diminish if f decreases). The latter might stem from the dependence of f^* on the effective added-mass (see e.g. Ref. [31]), which quantifies the effect of the total lift force in phase with the body acceleration, whose contribution increases with d/D at large U^*. Besides, the fact that $f^* < 1$ prevents the jump in phase ϕ for $d/D = 0.32$ and 0.4, which remains close to 0^o at large U^*. This behaviour, however, can be also related to changes in the cross-sectional arrangement of the cylinder, in this case with "a triangular shape", or to a stronger three-dimensionality of the shedding process. For instance, a comparable phenomenon has been recently reported for triangular prisms [32], or for a cylinder with helical strakes [33], where oscillation frequency remains always below the natural one, and no phase jump occurs.

Finally, a less complex forcing scenario is observed in Fig. 10(c) for configuration #2. Thus, when $d/D = 0.12$, the periodogram shows a similar forcing pattern to that corresponding to configuration #1, whereby the lock-in range is limited to $U^* < 11$, from which the dominant forcing frequency starts to follow again the natural shedding frequency. Concerning the initial branch, the lowest value of U^* presents now $f^* \simeq 1$, which is a typical feature of an incipient initial branch with quasi-periodic behavior [27]. As d/D increases, there is a progressive rightwards shift of the different branches, in line with previous observations on the lift and the phase. Interestingly, for $d/D = 0.4$, the forcing and response frequencies present a clear lock-in for the initial branch with $f^* \simeq 1$. In contrast with the former layout #1, now the spectra are seemingly more periodic, suggesting a more orderly shedding in the controlled wake.

4.4. Drag coefficient

Lastly, we will evaluate the effect of control rods on the mean drag coefficient, $\overline{C}_x$, which will be computed using the time-averaged in-line force as:

$$\overline{C}_x = \frac{\overline{F_x}}{0.5\rho D L u_\infty^2}. \tag{8}$$

Fig. 11 displays the mean drag coefficient $\overline{C}_x$ as a function of the reduced velocity for controlled systems of different d/D and configuration #1 and #2, along with the plain cylinder case, which is shown for comparison.

In general, for the uncontrolled case, the drag coefficient is correlated to the VIV amplitude response (see Fig. 4a and 5a) presenting larger values of $\overline{C}_x$ along the upper branch, where the response is highest, and showing lower values at initial and lower branches, where the value is similar to those typically reported for static cylinders, at the same Re. For configuration #1 (Fig. 11a), the VIV amplitude reduction provided by the implementation of control rods with $d/D \geq 0.2$ is associated to very remarkable drag reductions in the upper branch and lock-in range. In particular, for $d/D = 0.4$, the nearly suppressed VIV response for $U^* < 8$ leads to a maximum drag reduction of approximately 60%, which is considerably larger than other VIV control solutions studied in the past [11, 26]. These results could be expected from the small lift coefficient values displayed in Fig. 8, which were an indication of the lower vortex intensity at the wake. Such an effect would then translate into a larger base pressure in the vicinity of control rods, and therefore, into a smaller drag coefficient.

For layout #2, the situation is however different as Fig. 11(b) shows. In general, drag coefficient curves are displaced to larger values of reduced velocity as d/D grows, in line with what was observed for the VIV amplitude response. Besides, there is an important drag reduction at the upper branch for $d/D = 0.12$ and 0.2, that seems to be reverted for $d/D = 0.32$ and, more importantly, for $d/D = 0.4$, whose rightward shift and lock-in range widening leads to an important increase of drag for $U^* > 8$. Therefore, it seems evident that configuration #1 constitutes a more interesting control solution, not only in terms of amplitude response, but also for drag reduction.

5. Conclusions

We have presented an experimental study on the attenuation of vortex-induced vibration (VIV) of a low mass-damping one-degree-of-freedom circular cylinder, of diameter D, subject to uniform cross-flow, using pairs of control rods of varying size located in the near wake. Two different *optimal* layouts for control rods have been selected using recently obtained maps of VIV sensitivity to localized perturbations (Fig. 1). Both control symmetric configurations are based on a pair of rods at downstream distances of $r \simeq 0.9D$ (layout #1) and $r \simeq 1.3D$ (layout #2). Several values of the control cylinder diameter d have been tested, including $d = 0.12D$, $0.2D$, $0.32D$ and $0.4D$. Thus, although important amplitude reductions are observed for all arrangement investigated (Figs. 4 and 5), control solutions based on configuration #1 have been shown to provide with the largest mitigation of VIV amplitude response, reaching values of amplitude reduction of approximately 90% within the lock-in range.

Force measurements have been used to describe the nature of the changes in the wake and to shed some light on the physical mechanisms behind the VIV control. Therefore, the aforementioned strong reductions have been shown to be related to an important weakening of lift coefficient and phase modifications (Figs. 8 and 9). Additionally, the evaluation of drag coefficient implies that, for some particular arrangements, the amplitude response attenuations comes with a relevant drag reduction (especially at the upper branch), which in the case of layout #1 and $d = 0.4D$ is approximately 60%.

It is worth highlighting that such strong reduction in amplitude may be solely related to wake modifications induced by control rods, since, as it has been shown in Table 1, the increase of d/D was accompanied by a slight, progressive reduction of mass ratio m^* (and mass-damping ratio $m^*\xi$). Consequently, in view of other classical studies on the "Griffin" plot for the plain cylinder (see e.g. [34]), a less attenuated amplitude response should be expected if no wake control effects were put into play. Such effects seem to be related to sufficiently large control rods preventing the shear layers to roll in shortly behind the cylinder, thus reducing the magnitude of vortices in the near wake and consequently, the total lift and drag magnitudes. Besides, as occurs for cylinder with strakes or bumps [9], the control rods of increasing size may also act strengthening the wake three-dimensionality, subsequently leading to a weaker correlated vortex shedding, and a less coherent forcing. This hypothesis is supported by the observation of less periodic coherence and irregularity that forces time evolution display as d/D increases (signals are not shown here for the sake of brevity), that translates into spectra with multiple frequencies. This is especially remarkable for arrangements with layout #1, as Fig. 10(b) depicts.

In summary, the present strategy, based on optimal locations selected by means of sensitivity maps, has been proven to provide with significant VIV amplitude attenuation in combination with considerable drag reductions, a feature that can be considered of practical relevance in many engineering applications where

ensembles of several cylinders, subject to uniform cross-flow, need to be installed together.

Acknowledgements

This work has been supported by the Spanish MINECO (Subdirección General de Gestión de Ayudas a la Investigación and Agencia Estatal de Investigación) and European Funds under Projects DPI2017-89746-R and DPI2015-71645-P.

References

[1] P. W. Bearman, Vortex shedding from oscillating bluff bodies, Annu. Rev. Fluid Mech. 16 (1) (1984) 195–222. doi:10.1146/annurev.fl.16.010184.001211.

[2] B. Sumer, J. Fredsoe, Hydrodynamics around cylindrical structures, Vol. 26 of Advanced Series on Ocean Engineering, World Scientific, 1997.

[3] S. Mittal, V. Kumar, Flow-induced vibrations of a light circular cylinder at reynolds numbers 10^3 to 10^4, J. Sound Vib. 245 (5) (2001) 923 – 946. doi:https://doi.org/10.1006/jsvi.2001.3612.

[4] T. Sarpkaya, A critical review of the intrinsic nature of vortex-induced vibrations, J. Fluids Struct. 19 (4) (2004) 389 – 447. doi:https://doi.org/10.1016/j.jfluidstructs.2004.02.005.

[5] C. H. K. Williamson, , R. Govardhan, Vortex-induced vibrations, Annu. Rev. Fluid Mech. 36 (1) (2004) 413–455. doi:10.1146/annurev.fluid.36.050802.122128.

[6] R. G. Gabbai, H. Benaroya, An overview of modeling and experiments of vortex-induced vibration of circular cylinders, J. Sound Vib. 282 (3) (2005) 575 – 616. doi:https://doi.org/10.1016/j.jsv.2004.04.017.

[7] P. W. Bearman, Circular cylinder wakes and vortex-induced vibrations, J. Fluids Struct. 27 (5) (2011) 648 – 658. doi:https://doi.org/10.1016/j.jfluidstructs.2011.03.021.

[8] H. Choi, W.-P. Jeon, J. Kim, Control of flow over a bluff body, Annu. Rev. Fluid Mech. 40 (1) (2008) 113–139. doi:10.1146/annurev.fluid.39.050905.110149.

[9] M. M. Zdravkovich, Review and classification of various aerodynamic and hydrodynamic means for suppressing vortex shedding, J Wind Eng. Ind. Aero. 7 (2) (1981) 145 – 189. doi:https://doi.org/10.1016/0167-6105(81)90036-2.

[10] R. D. Blevins, Flow-Induced Vibration, 2nd Edition, Van Nostrand Reinhold, 1990.

[11] G. R. S. Assi, P. W. Bearman, N. Kitney, Low drag solutions for suppressing vortex-induced vibration of circular cylinders, J. Fluids Struct. 25 (4) (2009) 666 – 675. doi:https://doi.org/10.1016/j.jfluidstructs.2008.11.002.

[12] F. J. Huera-Huarte, On splitter plate coverage for suppression of vortex-induced vibrations of flexible cylinders, Appl. Ocean Res. 48 (2014) 244 – 249. doi:https://doi.org/10.1016/j.apor.2014.09.002.

[13] P. Bearman, M. Brankovic, Experimental studies of passive control of vortex-induced vibration, Eur. J. Mech. B/Fluids 23 (1) (2004) 9 – 15. doi:https://doi.org/10.1016/j.euromechflu.2003.06.002.

[14] T. Zhou, S. F. Mohd. Razali, Z. Hao, L. Cheng, On the study of vortex-induced vibration of a cylinder with helical strakes, J. Fluids Struct. 27 (7) (2011) 903 – 917. doi:https://doi.org/10.1016/j.jfluidstructs.2011.04.014.

[15] M. Rahmanian, M. Zhao, L. Cheng, T. Zhou, Two-degree-of-freedom vortex-induced vibration of two mechanically coupled cylinders of different diameters in steady current, J. Fluids Struct. 35 (2012) 133 – 159. doi:https://doi.org/10.1016/j.jfluidstructs.2012.07.001.

[16] I. Korkischko, J. R. Meneghini, Suppression of vortex-induced vibration using moving surface boundary-layer control, J. Fluids Struct. 34 (2012) 259 – 270. doi:https://doi.org/10.1016/j.jfluidstructs.2012.05.010.

[17] L. A. R. Quadrante, Y. Nishi, Amplification/suppression of flow-induced motions of an elastically mounted circular cylinder by attaching tripping wires, J. Fluids Struct. 48 (2014) 93 – 102. doi:https://doi.org/10.1016/j.jfluidstructs.2014.02.018.

[18] H. Zhu, J. Yao, Y. Ma, H. Zhao, Y. Tang, Simultaneous cfd evaluation of viv suppression using smaller control cylinders, J. Fluids Struct. 57 (2015) 66 – 80. doi:https://doi.org/10.1016/j.jfluidstructs.2015.05.011.

[19] H. Wu, D. P. Sun, L. Lu, B. Teng, G. Q. Tang, J. N. Song, Experimental investigation on the suppression of vortex-induced vibration of long flexible riser by multiple control rods, J. Fluids Struct. 30 (2012) 115 – 132. doi:https://doi.org/10.1016/j.jfluidstructs.2012.02.004.

[20] M. Lou, P. Chen, Z. Chen, Experimental investigation on the suppression of vortex-induced vibration of two interfering risers by control rods, Ships Offshore Struc. 12 (8) (2017) 1117–1126. doi:10.1080/17445302.2017.1316558.

[21] H. Zhu, J. Yao, Numerical evaluation of passive control of viv by small control rods, Appl. Ocean Res. 51 (2015) 93 – 116. doi:https://doi.org/10.1016/j.apor.2015.03.003.

[22] P. J. Strykowski, K. R. Sreenivasan, On the formation and suppression of vortex shedding at low reynolds numbers, J. Fluid Mech. 218 (1990) 71–107. doi:10.1017/S0022112090000933.

[23] H. Sakamoto, H. Haniu, Optimum suppression of fluid forces acting on a circular cylinder, J. Fluids Eng. 116 (2) (1994) 221–227. doi:doi:10.1115/1.2910258.

[24] C. Dalton, Y. Xu, J. C. Owen, The suppression of lift on a circular cylinder due to vortex shedding at moderate reynolds numbers, J. Fluids Struct. 15 (3) (2001) 617 – 628. doi:https://doi.org/10.1006/jfls.2000.0361.

[25] J.I. Jiménez-González, F. J. Huera-Huarte, Experimental sensitivity of vortex-induced vibrations to localized wake perturbations, J. Fluids Struct. 74 (2017) 53 – 63. doi:https://doi.org/10.1016/j.jfluidstructs.2017.07.010.

[26] F. J. Huera-Huarte, Suppression of vortex-induced vibration in low mass-damping circular cylinders using wire meshes, Mar. Struct. 55 (2017) 200 – 213. doi:https://doi.org/10.1016/j.marstruc.2017.05.008.

[27] A. Khalak, C. H. K. Williamson, Motions, forces and mode transitions in vortex-induced vibrations at low mass-damping, J. Fluids Struct. 13 (7) (1999) 813 – 851. doi:https://doi.org/10.1006/jfls.1999.0236.
[28] R. Govardhan, C. H. K. Williamson, Modes of vortex formation and frequency response of a freely vibrating cylinder, J. Fluid Mech. 420 (2000) 85 – 130. doi:10.1017/S0022112000001233.
[29] B. Seyed-Aghazadeh, D. W. Carlson, Y. Modarres-Sadeghi, The influence of taper ratio on vortex-induced vibration of tapered cylinders in the crossflow direction, J. Fluids Struct. 53 (2015) 84 – 95. doi:https://doi.org/10.1016/j.jfluidstructs.2014.07.014.
[30] R. Bourguet, D. Lo Jacono, Flow-induced vibrations of a rotating cylinder, J. Fluid Mech. 740 (2014) 342 – 380. doi.org/10.1017/jfm.2013.665
[31] M. Paidoussis, S. Price, E. de Langre, Fluid-Structure Interactions: Cross-Flow-Induced Instabilities, Cambridge University Press, 2011.
[32] B. Seyed-Aghazadeh, D. W. Carlson, Y. Modarres-Sadeghi, Vortex-induced vibration and galloping of prisms with triangular cross-sections, J. Fluid Mech. 817 (2017) 590 – 618. doi:10.1017/jfm.2017.119.
[33] M. Brankovic, P. W. Bearman, Measurements of transverse forces on circular cylinders undergoing vortex-induced vibration, J. Fluids Struct. 22 (6) (2006) 829 – 836. doi:https://doi.org/10.1016/j.jfluidstructs.2006.04.022.
[34] R. A. Skop, S. Balasubramanian, A new twist on an old model for vortex-excited vibrations, J. Fluids Struct. 11 (4) (1997) 395 – 412. doi:https://doi.org/10.1006/jfls.1997.0085.